ELSEVIER

Magnetic Resonance Imaging 18 (2000) 525–535

MAGNETIC RESONANCE IMAGING

Detection of areas with viable remnant tumor in postchemotherapy patients with Ewing's sarcoma by dynamic contrast-enhanced MRI using pharmacokinetic modeling

Michael Egmont-Petersen[a,*], Pancras C.W. Hogendoorn[c], Rob J. van der Geest[a], Henri A. Vrooman[a], Henk-Jan van der Woude[b], Jasper P. Janssen[a], Johan L. Bloem[b], Johan H.C. Reiber[a]

[a]*Division of Image Processing (Dept. of Radiology), Leiden University Medical Center, P.O.B. 9600, 2300 RC Leiden, The Netherlands*
[b]*Department of Radiology, Leiden University Medical Center, P.O.B. 9600, 2300 RC Leiden, The Netherlands*
[c]*Deptartment of Pathology, Leiden University Medical Center, P.O.B. 9600, 2300 RC Leiden, The Netherlands*

Received 15 August 1999; accepted 23 February 2000

Abstract

An approach is presented for monitoring the effects of neoadjuvant chemotherapy in patients with Ewing's sarcoma using dynamic contrast-enhanced perfusion magnetic resonance (MR) images. For that purpose, we modify the three-compartment pharmacokinetic permeability model introduced by Tofts et al. (Magn Reson Med 1991;17:357–67) to a two-compartment model. Perfusion MR images acquired using an intravenous injection with Gadolinium (Gd-DTPA) are analyzed with this two-compartment pharmacokinetic model as well as the with an extended pharmacokinetic model that includes the (local) arrival time t_0 of the tracer as an endogenous (estimated) parameter. For each MR section, a wash-in parameter associated with each voxel is estimated twice by fitting each of the two pharmacokinetic models to the dynamic MR signal. A comparison of the two wash-in parametric images (global versus local arrival time) with matched histologic macroslices demonstrates a good correspondence between areas with viable remnant tumor and a high wash-in rate. This can be explained by the high number and permeability of the (leaking) capillaries in viable tumor tissue. The novel pharmacokinetic model based on a local arrival time of tracer results in the best fit of the wash-in rate, the most important factor discerning viable from nonviable tumor components. However, parameter estimates obtained with this model are also more sensitive to noise in the MR signal. The novel pharmacokinetic model resulted in a sensitivity between 0.22 and 0.60 and a specificity between 0.61 and 1. The model based on a global arrival time gave sensitivities between 0.33 and 0.77 and specificities between 0.58 and 0.99. Both statistics are computed as the fraction of correctly labeled voxels (viable or nonviable tumor) within a specified ROI, which delineates the tumor. We conclude that the added value of estimating the local arrival time of tracer first manifests itself for moderate noise levels in the MR signal. The novel pharmacokinetic model should moreover be preferred when pharmacokinetic modeling is applied on the average signal intensity within a ROI, where noise has less effect on the fitted parameters.

Keywords: Pharmacokinetics; Two-compartment model; Local arrival time; Validation; Segmentation; Bone neoplasms; Ewing's sarcoma; Registration

1. Introduction

The diagnosis of bone sarcoma traditionally has been based on an integrated approach using clinical data, conventional radiography [1], and histopathology. Contrast-enhanced magnetic resonance imaging (MRI) has proven to be the method of choice for a proper estimation of the extent of bone tumors [2–4]. Contrast-enhanced MR imaging, however, does not allow an optimal estimation of the response to preoperative chemotherapy in the case of osteo- or Ewing's sarcoma [5], as this technique is unable to visualize small, scattered foci of residual tumor [6]. Dynamic contrast-enhanced MR imaging using an intravenous contrast tracer is a sensitive indicator for the presence of remnants of viable tumor in patients with high-grade osteosarcoma and Ewing's sarcoma sarcoma [5]. A dynamic MR sequence can be analyzed by drawing two Regions-of-Interest (ROIs), one around the tumor and another around the feeding artery.

* Corresponding author. Tel.: +1-31-71-5262285; fax: +1-31-71-5266801.

E-mail address: michael@lkeb.azl.nl (M. Egmont-Petersen).

0730-725X/00/$ – see front matter
PII: S0730-725X(00)00144-2

The average signal can be computed per ROI and rendered as a signal-enhancement curve. A study based on such a technique indicated that both the difference between the slopes of the two signal-enhancement curves and the difference between the arrival times of the tracer (in the artery and the lesion) correlated well with the malignant potential of the tumor as indicated by its histologic classification [3]. This ROI-based technique results in a high signal-to-noise ratio but at a coarse spatial resolution. The technique shows a high correlation with histology if the perfusion pattern of the tumor is homogenous, an assumption which is in most cases not fulfilled by malignant (postchemotherapy) bone tumors. Subtraction of dynamic contrast-enhanced MR images—MR-images before and after the arrival of contrast tracer—results in a high spatial resolution but is limited in the characterization of a continuous, ongoing process (perfusion) by solely one instantaneous measurement.

A local assessment of different parts of the lesion can be obtained by fitting a pharmacokinetic model to each voxel in the dynamic MR images. A pharmacokinetic model is a differential equation that specifies changes in concentration of a substance as a function of time in one or more compartments. In our application, it models the concentration of contrast tracer in the blood plasma and the extracellular compartments as a function of time.

In this article, we derive a two-compartment pharmacokinetic model based on the model introduced by Tofts et al. [7]. This two-compartment model is further modified by including the local arrival time of tracer as a fitted parameter. For each voxel, a two-compartment pharmacokinetic model is fitted such that the model parameters characterize salient features of the dynamic MR signal. Corresponding to each model parameter, a so-called parametric image is composed. The parametric images indicate the local wash-in (tracer uptake), the local wash-out (tracer elimination), the local arrival time of the blood (t_0) and the local maximal enhancement (a) caused by the uptake of contrast tracer in the tumor. We have correlated these parametric images with the occurrence of residual viable tumor tissue in a matched histologic macro-section.

2. Materials and methods

2.1. Subjects

In our study, eight consecutive patients with Ewing's sarcoma who underwent neoadjuvant chemotherapy were selected. For each patient, a pathologic specimen was available after surgery which could be matched with the results from the preoperative MR examination. Table 1 lists the gender, age, location of tumor and response to chemotherapy for each patient. The patients, five males and three females, ranging in age from 3 to 21 years (mean = 15 years) underwent neoadjuvant chemotherapy according to the protocols of the Cooperative Ewing Sarcoma Study [8].

Table 1
Study subjects

Index	Gender	Age	Location	Response	Average size, viable tumor
1	Male	14	Femur	I	23 voxels
2	Male	14	Fibula	II	8 voxels
3	Female	21	Femur	II	16 voxels
4	Female	19	Fibula	II	26 voxels
5	Male	15	Tibia	III	6 voxels
6	Male	19	Femur	III	7 voxels
7	Female	18	Tibia	IIIa	0 voxels
8	Male	3	Femur	IIIa	0 voxels

Five males and three females, with Ewing's sarcoma were included in our study. The tumors were either located in the femur, fibula, or tibia. The response to chemotherapy was scored by two pathologists into one of four categories (see text). The average size of the islands with viable tumor was computed from the (registered) mask obtained from the histologic macro-slice.

The response to chemotherapy was assessed by two skilled pathologists according to the classification of histologic grades of tumor regression [9]. Four patients responded very well to chemotherapy (Class III/IIIa), three patients showed a moderate response (Class II) and one patient had a poor response (Class I).

2.2. MR imaging

After completion of preoperative chemotherapy, the MR examination was performed on a 0.5 T super-conductive Gyroscan (Philips, Best, the Netherlands) using a surface coil. Depending on the size of the tumor, one, two or three sections were selected for T_1-weighted dynamic contrast-enhanced imaging using a magnetization prepared imaging gradient recalled echo technique. The MR images were acquired with a repetition time (TR) of 12 ms (independent of the number of sections 1–3), an echo time (TE) of 5.7 ms, and a prepulse delay time of 741 ms. The flip angle was 30 degrees. The field-of-view varied per patient depending on the size of the tumor (200−450 mm). Images were acquired with a matrix size of 256 × 256 voxels. The slice thickness was 8 mm and the slice gap 12 mm. An intravenous bolus injection of the contrast tracer Gd-DTPA (Magnevist®) was given followed by a saline flush. For each MR section, 47 to 60 dynamic images were acquired with a temporal resolution of 3.3 s.

2.3. Pharmacokinetic analysis

A two-compartment model was derived and used to differentiate viable from non-viable tumor, see Fig. 1. The presence of contrast tracer in heavily vascularized tissue causes local magnetic field fluctuations which result in reduced relaxation times T_1 and T_2 [10]. Assuming that the transient reduction of the T_2 relaxation time can be neglected, the longitudinal relaxation is (in steady state) lin-

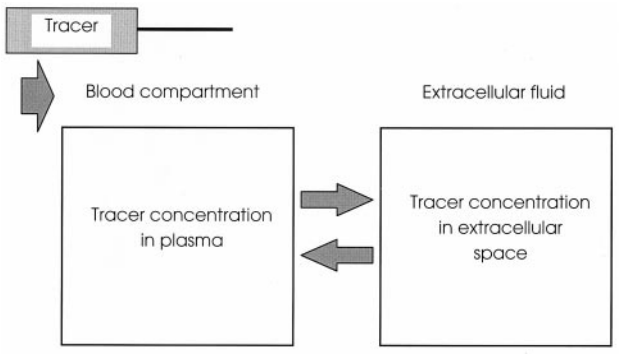

Fig. 1. This compartmental diagram indicates the exchange of blood (tracer) between the blood and extracellular compartment located in the tumor. The bolus with tracer is injected into the blood plasma. Thereafter, the differences in tracer concentration between the blood and extracellular compartments determine the net flow of tracer between the two compartments. For simplicity, secretion to the kidneys has been omitted.

early related to the tracer concentration C in tissue (tumor) via the bulk longitudinal relaxation time of blood [11]

$$\frac{1}{T_{1(c)}} = \frac{1}{T_1} + \alpha C \tag{1}$$

with T_1 the relaxation time of tissue in the absence of tracer and α the tissue- and frequency-dependent relaxivity. The signal intensity after the tracer has arrived obeys the following proportionality:

$$s(x, y, z) \propto (1 - e^{TR/T_{1(c)}}) \tag{2}$$

with TR being the repetition time. For small variations in $T_{1(c)}$, this exponential function can be approximated by a linear equation as a function of tracer concentration

$$s(x, y, z) = s_0(x, y, z) + \beta C \tag{3}$$

with $s_0(x, y, z)$ the signal intensity in the absence of tracer.

For a model with one compartment and secretion via the kidneys, the concentration of tracer in blood, C_b, as a function of time t after the injection of a bolus, is characterized by the differential equation [11,12]

$$\frac{dC_b}{dt} = -\frac{k_2}{V_b} C_b \qquad C_b(t) = e^{-(k_2/V_b)t} \tag{4}$$

with k_2 being the half-life of the bolus until renal secretion (thin curve in Fig. 2) and V_b the volume of blood plasma. When the exchange of tracer between the plasma compartment and the extracellular space is taken into account, the flow from the plasma to the extracellular space and the kidneys is captured by the differential equation [7]:

$$\frac{dC_b}{dt} = -\frac{k_1}{V_b}(C_b - C_e) - \frac{k_2}{V_b} C_b \tag{5}$$

with k_1 the transfer rate from the blood to the extracellular space and C_e the concentration of tracer in the extracellular compartment. The concentration of tracer in the extracellular compartment is given by:

$$\frac{dC_e}{dt} = \frac{k_1}{V_e}(C_b - C_e) \tag{6}$$

with k_1 the transfer rate from the blood to the extracellular space. The solution to these differential equations is derived in appendix A, and can for the blood compartment be described as follows:

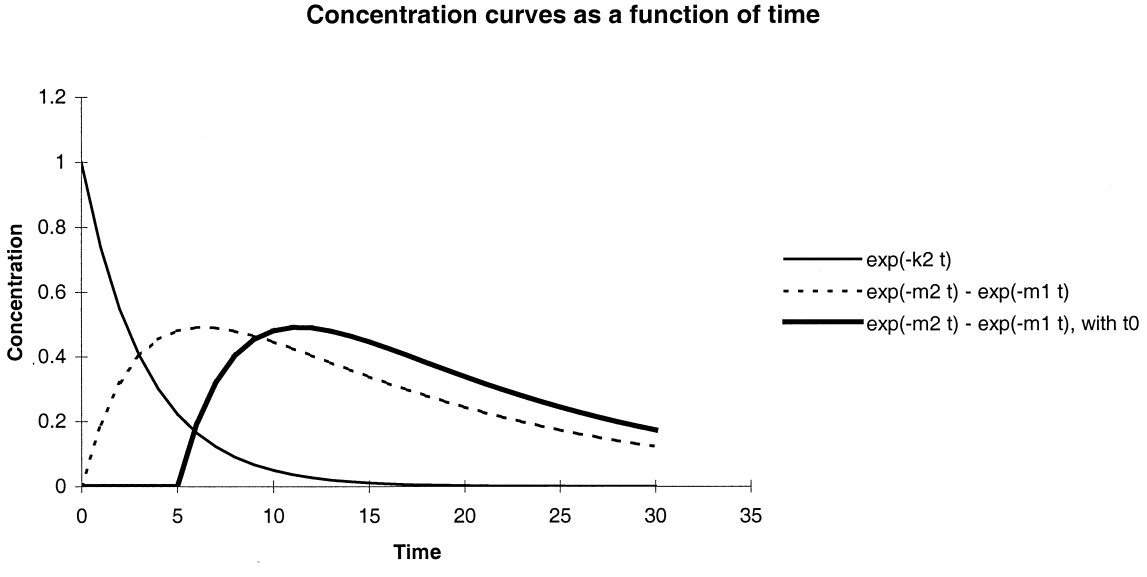

Fig. 2. The thin curve depicts the concentration of tracer as a function of time in the one-compartment model (solely wash-out). The dotted curve indicates the concentration of tracer according to the two-compartment model based on a global arrival time of tracer, $C_b(0) = 0$ (arrival time). The bold curve depicts the concentration of tracer for the novel two-compartment model with a local (estimated) arrival time $t_0 \geq 0$.

$$C_b(t) \cong D \frac{V_e}{V_b(V_b + V_e)} \exp\left(-\frac{k_1(V_b + V_e)}{V_b V_e} t\right) + h \quad (7)$$

with D the dose of the bolus, h a constant and V_e the volume of the extracellular water. Such an exponential function is a proper characterization of the concentration C_b as a function of time under the assumption of an instantaneous arrival of the bolus [13].

The solution to the differential equation (6), which is derived in Appendix B, yields

$$C_e(t) \cong a(e^{-m_2 t} - e^{-m_1 t}) \quad (8)$$

with m_1 and m_2 the wash-in and wash-out rates, respectively, defined as yields

$$m_1 = 2\frac{k}{v_e} \quad (9)$$

$$m_2 = \frac{k_1(V_p + V_e)}{V_b V_e}$$

with v_e the fraction of heavily vascularized tissue.

We will now extend the pharmacokinetic model to cope with the local arrival time of the tracer t_0. Implicit estimation of the arrival time of tracer has previously been included in pharmacokinetic models that were developed for analysis of measurements of the cerebral blood flow in PET images. Meyer extended a perfusion model with a delay correction using the factor Δt [14]. In Meyer's approach, the local arrival time is modeled by a convolution of the concentration function by an exponential term. We are not interested in modeling the arrival time as a dispersion of the bolus over time. Instead, we consider the local arrival time as a translation of the pharmacokinetic curve along the time axis. In the simple case where the infusion of contrast tracer occurs instantaneously, the arrival of tracer can be modeled by a local Dirac pulse and the tracer concentration by a step function, which cannot be differentiated for $t = t_0$. We chose to approximate the step function by

$$\lim_{g\to\infty} \frac{dC}{dt} = -gC(1 - C) \quad (10)$$

$$\lim_{g\to\infty} C(t) = \frac{1}{1 + e^{-g(t-t_0)}}$$

which is differentiable for $|g| \neq \infty$. Note that the length of the time interval over which the tracer is administered is not taken into account. Taking the product between Eq. (8) and (10) yields

$$C_e(t) = \frac{1}{1 + e^{-g(t-t_0)}} a(e^{-m_2(t-t_0)} - e^{-m_1(t-t_0)}) \quad (11)$$

(bold curve in Fig. 2). The two-compartment model, Eq. (11), is extended with the (average) signal amplitude before tracer has arrived $\bar{s}_0(x, y, z)$ yielding the stochastic model

$$C_e(t) = \bar{s}_0(x, y, z) + \frac{a}{1 + e^{-g(t-t_0)}} (e^{-m_2(t-t_0)} - e^{-m_1(t-t_0)}) + \varepsilon(x, y, z) \quad (12)$$

The parameters of the pharmacokinetic model defined in Eq. (12), $\bar{s}_0(x, y, z)$, a, t_0, m_1 and m_2, can be estimated for each voxel (x, y, z) by minimizing the residual error $\varepsilon(x, y, z)$. This model will be compared with a pharmacokinetic model based on a *global* estimation of the arrival time $\bar{t}_0$

$$C'_e(t) = s_0(x, y, z) + a'[e^{-m'_2 t} - e^{-m'_1 t}] + \varepsilon'(x, y, z), \qquad t \geq \bar{t}_0 \quad (13)$$

In this pharmacokinetic model, the initial signal intensity $s_0(x, y, z)$ equals the signal intensity at time $t' = \bar{t}_0$.

2.4. Comparison with a postoperative histologic macroslice

Following surgery, the tumor resection was analyzed histologically. A so-called macro slice, of which the position and orientation corresponded exactly with one of the dynamic MR-slices, was sectioned as described previously [15]. This histologic slice indicates which areas contain remnants of viable tumor as they are characterized by a high affinity for Hematoxylin (small blue round cell tumor) which renders an intense pink/blue color (see the dark 'islands' in Fig. 3a).

The histologic macroslice was digitized on a high-quality color scanner (600 dpi). Before it could be used as a reference, the histologic image needed to be matched spatially with the appropriate MR section. This registration was performed by delineating structures that were clearly visible in both the T_1-weighted MR images and the histologic slice. Two geometrically congruent contours specifying either the silhouette of the bone cortex or large regions with normal bone marrow were drawn manually, one in the (digitized) histologic image and the other in the T_1-weighted MR image. The differences in scale, orientation and position between the contours were computed as specified in Appendix C. Fig. 3 shows the matched contours. The histologic image was subsequently scaled, rotated and translated to the correct position.

The areas containing viable tumor in the histologic macroslice were enhanced as follows: The average RGB-intensity vector was computed from the pixels within one remnant with viable tumor, $\bar{p}(x, y)$. Pixels with a color-spectrum resembling $\bar{p}(x, y)$ are very likely to belong to an area with viable tumor. We computed the correlation $r(x, y)$ between $\bar{p}(x, y)$ and each pixel vector $p(x, y)$ in the digitized (RGB) histologic image

$$r(x, y) = \frac{\bar{p}(x, y) \cdot p(x, y)}{|\bar{p}(x, y)| \cdot |p(x, y)|} \quad (14)$$

with $|\cdot|$ the vector norm. The correlation measure $r(x, y)$ indicates the similarity between the RGB colors of two

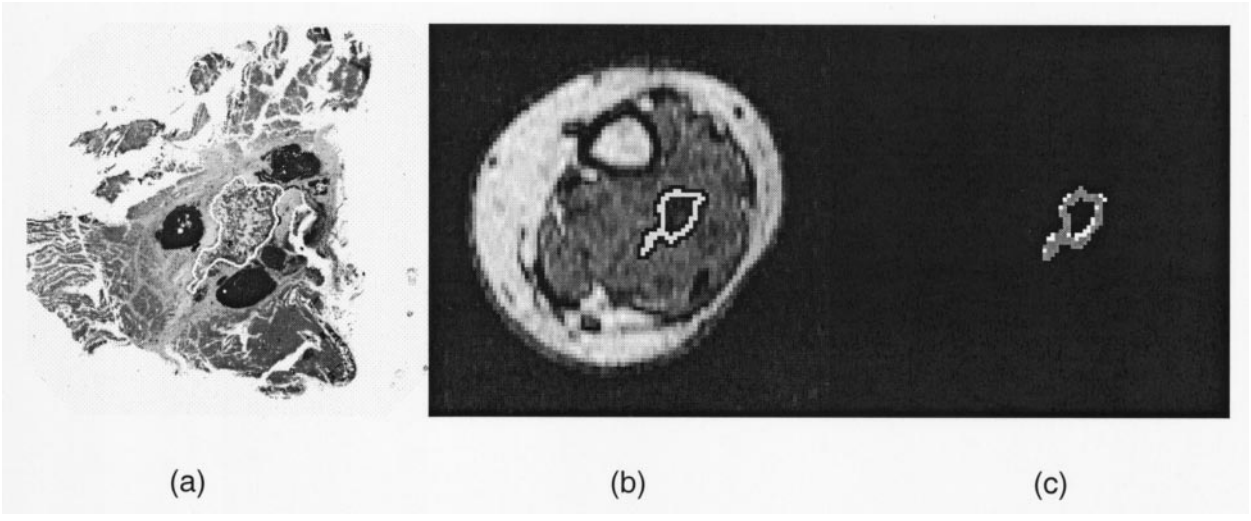

Fig. 3. A (white) contour has been drawn around bone cortex in the digitized histologic macroslice (a). The T_1-weighted MR image (b) contains the corresponding, manually drawn contour. (c) shows the match of the two contours computed as specified in Appendix C.

pixels and is independent of their signal intensity. From Eq. (14), a gray-level image is composed in which the intensity of pixel (x, y) equals $r(x, y)$. By applying the optimal threshold on this image, areas with a high density of cancerous cells are separated from the remaining tissues and from bone cortex. This resulted in a (registered) mask in which the white pixels indicate areas with viable tumor. Each mask image was verified by an experienced pathologist and the volume of viable tumor was compared with the estimate obtained from the pathological analysis of the specimen.

The parametric images were computed for the MR section that corresponded with the histologic macroslice. Each parametric image computed from the dynamic MR images of the same patient was compared with the corresponding mask as follows. First, a ROI that demarcated the whole tumor within the MR slice (time $t = 0$) was drawn manually (note that the choice of ROI is likely to influence the estimated sensitivity and specificity of our approach). The parameters of the pharmacokinetic models, Eq. (12) and Eq. (13), were estimated by nonlinear regression. The moment of acquisition of the MR image preceding the first MR image in which the arrival of tracer could be visually identified, was chosen as the global arrival time $\bar{t}_0$ in Eq. (13). The other parameters in the two pharmacokinetic models were estimated using the Levenberg–Marquart algorithm [16], which minimizes the residual errors. This algorithm switches continuously between a first-order steepest descent method and a second-order method based on the Hessian matrix. The Levenberg–Marquart algorithm requires no parameters to be specified as only the maximal number of iterations needs to be chosen in advance. Preliminary experiments had indicated that the residual error changed little after 20–30 iterations, so we decided to terminate the algorithm after 50 iterations. The initial parameter settings of the pharmacokinetic model were chosen such that they resembled the characteristics of viable tumor. This prevented the fitting algorithm from ending up in local minima when fitted on MR signals obtained from viable tumor voxels.

Seven parametric images, *wash-in* $m_1(x, y, z)$ and $m_1'(x, y, z)$, *amplitude* $a(x, y, z)$ and $a'(x, y, z)$, *wash-out* $m_2(x, y, z)$ and $m_2'(x, y, z)$, and *local arrival time* $t_0(x, y, z)$, were composed. All the parametric images were postprocessed with a 3×3 median filter to remove outliers. The parametric images computed from the pharmacokinetic model Eq. (12) were compared with the parametric images computed from the model based on a global arrival time of the contrast, Eq. (13).

2.5. Statistical analysis

For each patient, the classification (thresholding) of each voxel in the wash-in parametric image (viable or nonviable tumor) was compared with the correct labeling as specified by the mask that was derived from the corresponding histologic macroslice. The segmentation result was assessed with the following quality measures: overall correctness ρ, class-conditional correctness given the true class $\rho(\textit{viable})$ and $\rho(\textit{rest tumor})$ as well as the quality measure kappa (κ). Given a 2×2 contingency table Q

Classified as	Mask		
	Viable	Rest tumor	Total
Viable	$q_{1,1}$	$q_{1,2}$	$q_{1,\cdot}$
Rest tumor	$q_{2,1}$	$q_{2,2}$	$q_{2,\cdot}$
Total	$q_{\cdot,1}$	$q_{\cdot,2}$	$q_{\cdot,\cdot}$

the quality measures are defined as follows:

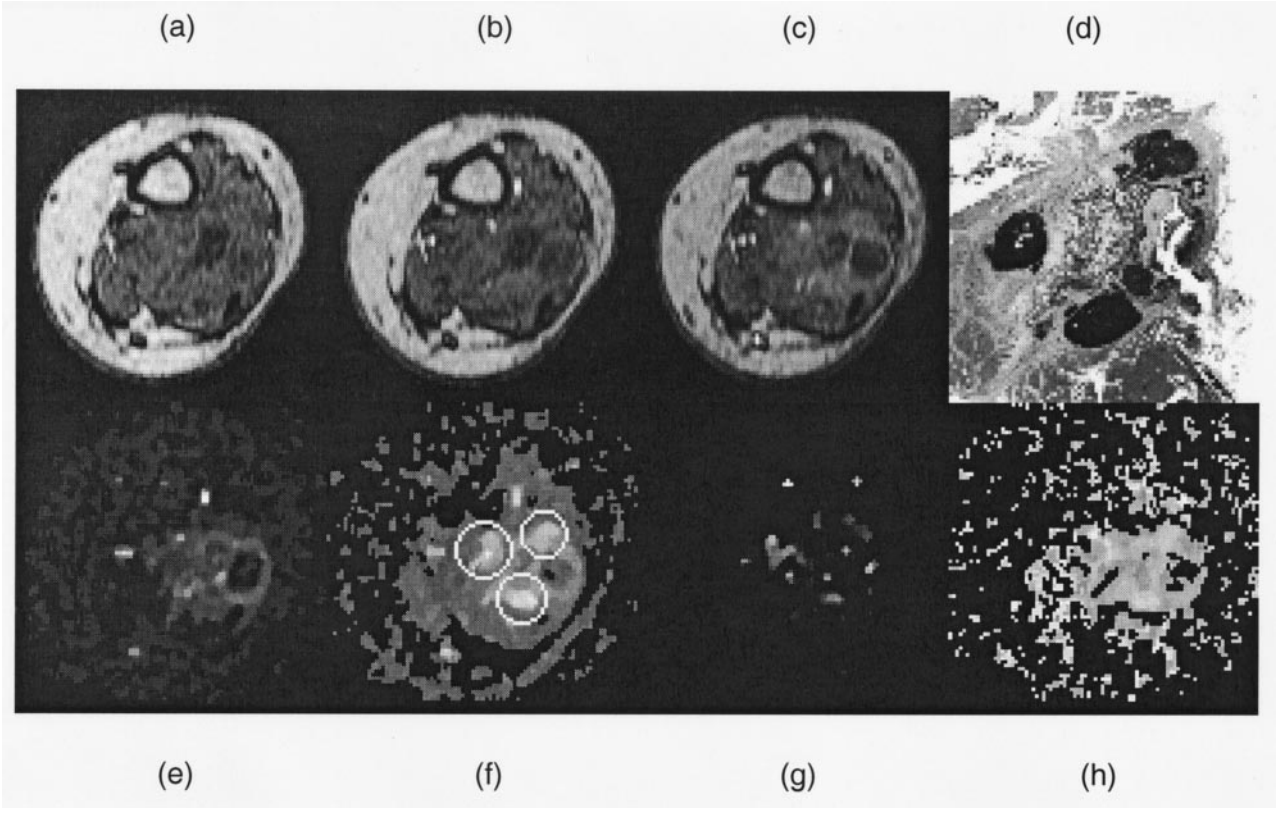

Fig. 4. (a) T_1-weighted dynamic MR image before the arrival of tracer, (b) when the tracer has just arrived and (c) 10 s after the arrival of tracer. (d) shows the histologic macroslice, which is rotated such that its orientation matches that of the MR section. (e–h) show the parametric images: (e) maximal enhancement, (f) wash-in, (g) wash-out and (h) local arrival time. The (dark) remnants of viable tumor in the histologic macroslice (d) can be located in the wash-in parametric image (f).

correctness

$$\rho = \frac{q_{1,1} + q_{2,2}}{q_{\bullet,\bullet}} \tag{15}$$

class-conditional correctness *viable tumor* (sensitivity)

$$\rho(viable) = \frac{q_{1,1}}{q_{\bullet,1}} \tag{16}$$

class-conditional correctness *rest tumor* (specificity)

$$\rho(rest\ tumor) = \frac{q_{2,2}}{q_{\bullet,2}} \tag{17}$$

and the inter-observer measure kappa

$$\kappa = \frac{\rho - \lambda}{1 - \lambda} \tag{18}$$

with

$$\lambda = \frac{q_{1,\bullet} \times q_{\bullet,1} + q_{2,\bullet} \times q_{\bullet,2}}{q_{\bullet,\bullet}^2} \tag{19}$$

These quality measures were thoroughly discussed earlier [17] and their confidence intervals were given.

For each patient, the kappa-correspondence between the mask image (indicating voxels located in remnants with viable tumor) and each of the two wash-in parametric images, $m_1(x, y, z)$ and $m_1'(x, y, z)$, was computed for different values of a threshold θ. All voxels in the wash-in image (within the defined ROI) with an intensity larger than this threshold, $m_1(x, y, z) > \theta$ or $m_1'(x, y, z) > \theta'$, were considered viable tumor, the other voxels within the ROI as nonviable tumor. The threshold value that resulted in the highest agreement (maximal κ) indicated the classification result which was used to compute the other quality measures: ρ, $\rho(viable)$ and $\rho(rest\ tumor)$.

3. Results

For seven patients, bone cortex was used to match the MR and histologic images whereas for one patient the borders between the (intraosseous) tumor and the healthy tissue were used for matching. The difference in scale between the MR and digitized histologic images varied between 4 and 10.5.

For each patient, parametric images were computed from the dynamic MR images of the appropriate slice. Fig. 4a shows an MR image before the contrast tracer has been administered, Fig. 4b shortly after the arrival of the bolus and Fig. 4c approximately 10 s after the arrival of the tracer in the chosen MR section. Fig. 4e–h show the four para-

Table 2
Kappa and class-conditional correctness of viable and rest tumor for local time of tracer

Patient	Kappa Corectness		C.c. correctness	
			Viable tumor	Rest tumor
1	0.38	0.80	0.60	0.84
2	0.06	0.61	0.63	0.61
3	0.10	0.81	0.55	0.81
4	0.38	0.79	0.43	0.91
5	0.20	0.98	0.22	0.99
6	0.21	0.93	0.45	0.94
7	–	0.98	–	0.98
8	–	1.00	–	1.00

The correspondence between the wash-in parametric image computed with the novel pharmacokinetic model (local arrival time of tracer) and the histologic macroslice. In two patients, no macroscopic remnants remained in the histologic macroslice so that the kappa and class-conditional (C.c.) correctness of viable tumor could not be computed.

metric images resulting from fitting using Eq. (12) to the signal obtained from each voxel. Note the correspondence between the dark 'islands' in the histologic macroslice (Fig. 4d) and the marked bright structures in the wash-in parametric image (Fig. 4f).

The results from computing the correctness and kappa-statistic per patient (within the defined ROI) are presented in Table 2 (Eq. (12)) and Table 3 (Eq. (13)). With respect to correctness, both pharmacokinetic models resulted in a similar performance for three patients whereas for five patients a higher correctness was obtained with the novel pharmacokinetic model based on a local arrival time of tracer. Consequently, the novel pharmacokinetic model classifies more or, in the worst case, as many voxels correctly as the model based on a global arrival time. So the novel model gives the most precise estimate of the volume of viable tumor. For two patients, the novel pharmacokinetic model resulted in a higher kappa-statistic than the model based on a global arrival time, while for four patients it resulted in lower kappa values. The reason why the novel pharmacokinetic model does not improve the diagnostic accuracy compared with the existing model is the presence of measurement noise. This is discussed in the subsequent section.

Table 3
Kappa and class-conditional correctness of viable and rest tumor for global time of tracer

Patient	Kappa Correctness		C.c. correctness	
			Viable tumor	Rest tumor
1	0.41	0.80	0.66	0.83
2	0.08	0.59	0.77	0.58
3	0.15	0.81	0.71	0.81
4	0.41	0.77	0.58	0.83
5	0.07	0.92	0.33	0.93
6	0.10	0.85	0.50	0.86
7	–	0.98	–	0.98
8	–	0.99	–	0.99

The correspondence between the wash-in parametric image computed with the pharmacokinetic model based on a global arrival time of tracer and the histologic macroslice. In two patients, no macroscopic remnants remained in the histologic macroslice so that the kappa and class-conditional correctness of viable tumor could not be computed.

Fig. 5 shows the relation with the average size of an 'island' with viable tumor in the mask image and the kappa value resulting from segmenting the associated parametric image. Clearly, the larger the remnants, the better the correspondence between the wash-in image $m_1'(x, y, z)$ and the histologic mask. The parametric images indicating maximal enhancement, $a(x, y, z)$, make a distinction possible between the areas with tumor (viable and nonviable tumor) and healthy tissue. Fig. 4e shows the maximal enhancement parametric image of a patient.

4. Discussion

We computed parametric images using the pharmacokinetic models based on a local and a global arrival time of tracer, respectively. Comparison with the matched histologic macroslice indicated that the wash-in parametric images are suited for identifying remnants of viable postchemotherapy tumor in patients with Ewing's sarcoma. The blood flow in the highly permeable (leaking) capillaries is high in viable tumor tissue whereas in the remaining parts of the postchemotherapy tumor, the blood supply is often less than in normal (musculoskeletal) tissue. Consequently, a high wash-in rate is to be expected for viable tumor tissue.

The pharmacokinetic model with local arrival time, Eq. (12), can in a certain way be seen as a simplification of the two-compartment model proposed by Hoffmann et al. [11]. Their model is henceforward called the infusion model because it models the injection of the bolus as a block signal. The fact that the injection of tracer is modeled this way, has the consequence that the infusion model is not differentiable in the point $t = \tau$. Since the Levenberg–Marquart method used for fitting the pharmacokinetic parameters entails an evaluation of all partial derivatives, the fitting procedure might oscillate. Another and more apparent disadvantage of pharmacokinetic models based on a manually specified global arrival time is that different users may disagree with respect to their choice of $\bar{t}_0$, the global arrival time, such that estimates of the wash-in rate and maximal enhancement become subject to inter-observer variation. In our novel pharmacokinetic model Eq. (12), the arrival time is estimated as an endogenous parameter which reduces the required user interaction to drawing the region of interest.

The parameter estimates of t_0 varied within ± 10 sec within a typical region of interest. In the t_0 parametric image computed with the novel model (Fig. 4h), it appears that the local tracer arrival time in a voxel located in nonviable tumor tissue (slow wash-in rate) precedes the arrival time in a voxel located within viable tumor (high wash-in

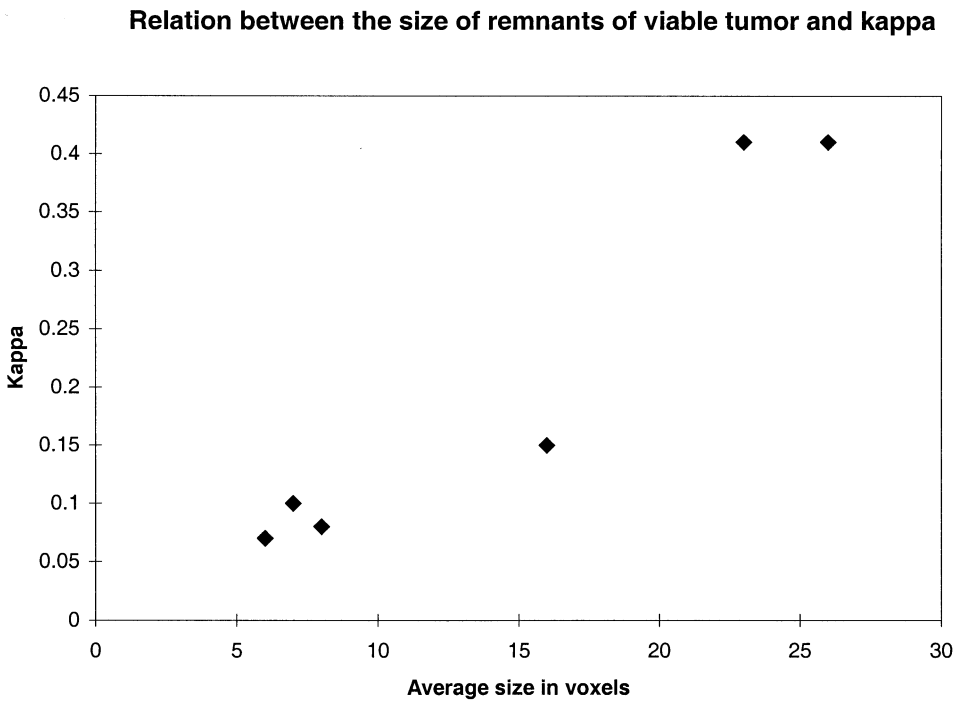

Fig. 5. The correspondence between the wash-in parameter and the location of viable tumor improves with the resolution in the MR images. The figure is based on the wash-in parameters computed with the pharmacokinetic model based on a global arrival time.

rate). This problem is caused by the fact that the Levenberg Marquart algorithm occasionally ends up in a local minimum when fitting the pharmacokinetic model Eq. (12) to an MR signal associated with nonviable tumor. Simulations have shown that the confidence of the parameter t_0 depends on the value of the wash-in parameter (slope) in Eq. (12). A higher wash-in rate m_1 implies a better confidence of the estimated t_0 parameter. How to minimize the risk of ending up in local minima resulting in biased parameter estimates, is a subject of future research.

The wash-in parameters estimated with the novel pharmacokinetic model, $m_1(x, y, z)$, fit the data better (resulting in a lower residual variance) than the wash-in parameters estimated with the model based on a global arrival time. As the wash-in rate is mainly determined by 3–5 subsequent observations (t_0 to $t_0 + 10$ seconds), the estimated wash-in rate is also more sensitive to noise. The main difference between the two pharmacokinetic models we used is that the local arrival time in Eq. (12) makes it possible to displace the nonlinear function along the time-axis (Fig. 1). This displacement results in a better fit of the up-slope viz. the wash-in rate. The pharmacokinetic model based on a global arrival time is less sensitive to changes in the slope associated with the wash-in rate, a fact that is confirmed by a smaller variance among the wash-in parameters, m_1', computed from Eq. (13)—global arrival time—than among the parameters, m_1, computed from Eq. (12). On the one hand, when the signal to noise ratio is good, a pharmacokinetic model is desired that is highly sensitive to the three to four observations that determine the wash-in coefficient. However, a more exact parameter fit increases the propagation of noise in the parameters. The noise level can be so high in the dynamic MR signal that a more rigid pharmacokinetic function is desired so the pharmacokinetic model with a global arrival time should be applied. When pharmacokinetic modeling is applied on the average signal intensity within a ROI, our novel pharmacokinetic model based on a local arrival time should certainly be preferred.

When estimating the parameters of the pharmacokinetic model with a global arrival time, Eq. (13), observations before the global arrival time $\bar{t}_0$ are removed. As the amplitude of the first observation ($t = \bar{t}_0$) is chosen as zero, an inappropriate choice of the arrival time will lead to biased estimates of the maximal enhancement a' and possibly also of the wash-in rate m_1'. Only the pharmacokinetic model with a local arrival time gives an unbiased estimate of the maximal enhancement a because no observations are abandoned.

Our experiments indicate that the pharmacokinetic parameter maximal enhancement, a, can be used to discern the tumor from the surrounding (healthy) tissue. Other perfusion studies have indicated that the relative enhancement of the T_1-weighted MR signal computed by a subtraction technique could not discriminate tumor from inflammatory tissue [18]. Animal experiments have shown that the signal increase in necrotic areas can be neglected [19]. Lyng et al. point out that the maximal enhancement of tissue depends on the fraction of heavily vascularized tissue in the extracellular space v_e [20], which is also evident from our pharmacokinetic model Eq. (B.6). However, we agree with Lyng et al. that the maximal signal enhancement is useful for a

comparison between tumors in situations where no absolute measure of perfusion is required.

In the present study, pharmacokinetic parameters estimated from preoperative dynamic MR images were compared with a histologic specimen obtained from subsequent surgery. By applying a threshold θ on the wash-in image, a classification of voxels into viable and nonviable tumor is obtained. Analyses of different patients indicate that the typical wash-in rate m_1 associated with viable tumor varies among the patients in our study. From the derivation of the pharmacokinetic model for the extracellular compartment, it is clear that m_1 is proportional to the product of the permeability P and the surface area per unit mass of tissue S, [see Eq. (B.1) in appendix B]. These two factors depend on the vascular properties of the local tissue, so we do not expect that one threshold θ value exists, which is optimal for all patients. It would be possible to obtain transversal histologic and MR sections (with a clearly visible artery) and compare the enhancement-signal of the voxels in the artery with the MR signal obtained from the voxels located in the tumor. However, such an approach would only allow compensation for varying bolus input functions, whereas the local permeability also is subject to inter- and intra-patient variation (intramedullar versus extramedullar tissue). A major disadvantage of a transversal orientation is that many more pathologic sections will be required to give a reliable estimate of the response to preoperative chemotherapy. Optimizing the thresholding procedure for successive MR examinations of the same patient during chemotherapy, is a subject of future research.

The wash-in parametric images are computed from an MR image sequence with a slice thickness of 8 mm, whereas the histologic specimen is 5 μm thin. It is clear that remnants with a diameter smaller than 8 mm do not occupy the whole MR slice, which results in partial volume effects. Consequently, remnants with a much larger diameter should show a better correspondence with histology than remnants with a diameter smaller than 8–12 mm. A scatter plot confirms such a relation between an increasing average size of an 'island' of viable tumor (cluster of 4-connected voxels in the binary mask image) and a higher kappa value.

In our study, the chosen ROI influences the results of our analysis. Whereas the remnants with viable tumor, in general, occur inside the ROI, the size of the ROI influences the number of voxels considered as nonviable tumor. Consequently, the estimated specificity ρ(nonviable) and the overall quality measures, κ and ρ, depend on the demarcation of the ROI. The sensitivity ρ(viable) depends to a much lesser extent on how the ROI is drawn. In the nearby future, we will investigate the intra- and interobserver variability of the area of viable tumor as depending on the specified ROI.

5. Conclusion

In this article, we have shown that areas with viable tumor can be discerned from areas with nonviable tumor by analyzing T_1-weighted dynamic contrast-enhanced MR images with a novel two-compartment pharmacokinetic model. As a result, the relative volume of viable tumor in patients with Ewing's sarcoma can be estimated during and after chemotherapy from the dynamic MR images. Compared with subtraction techniques, pharmacokinetic modeling has the advantage that the fitted parameters capture the dynamics of the perfusion process. Moreover, instead of fitting the pharmacokinetic parameters to the average intensity of a ROI, the parametric images give the highest possible spatial resolution. Comparison with a well-defined gold standard obtained from histology indicates a direct relation between a high wash-in rate and the presence of viable tumor. The larger the remnants the better the correspondence between viable tumor and wash-in rate.

The only difference between the pharmacokinetic models based on a global and a local (endogenous) arrival time is the extra parameter t_0 in the latter model. Consequently, the extended model is capable of better fitting the wash-in rate and maximal enhancement than a pharmacokinetic model based on a global arrival time. In general, the lower the noise level is in the dynamic MR signal, the more relevant it becomes to estimate the wash-in rate accurately. When, on the other hand, the noise level is relatively high a model based on a global arrival time smoothes the wash-in parameter estimates which in return become less sensitive to this noise. In our experiments with postchemotherapy Ewing's sarcoma, the novel pharmacokinetic model based on a local arrival time of tracer gave the best estimates of the number of voxels located within remnants with viable tumor. Finally, our novel pharmacokinetic model should be preferred when pharmacokinetic modeling is applied on the average signal intensity within a ROI where the noise has much less effect.

Acknowledgments

We wish to thank H.C. van Assen for his assistance with preparing this manuscript and the referees for valuable comments and suggestions. This project was financially supported by the Dutch Cancer Foundation (Koningin Wilhelmina Fonds), Grant no. RUL-97-1509.

Appendix A

The pharmacokinetic model for the blood compartment can be derived by writing Eq. (5) as

$$C_e = \frac{V_b}{k_1}\frac{dC_b}{dt} + \frac{k_2}{k_1}C_b + C_b \tag{A.1}$$

Substituting it for C_e in Eq. (6) yields the second order differential equation [7]

$$V_e V_b \frac{d^2 C_b}{dt^2} + (V_e k_2 + V_e k_1 + V_b k_1) \frac{dC_b}{dt} + k_1 k_2 C_b = 0 \tag{A.2}$$

(the polynomial $Qy'' + Ry' + U = 0$), with the solution

$$C_b(t) = Ae^{-m_2 t} + Be^{-m_3 t} \tag{A.3}$$

The roots to Eq. (A.3) are incomprehensible but taking into account that $k_1 \gg k_2$ [7], the solutions for m_2 and m_3 become

$$m_2 = \frac{k_1(V_b + V_e)}{V_b V_e} \qquad m_3 = \frac{k_2}{2V_b} \tag{A.4}$$

The coefficients A and B can be determined when the constraints $C_b(0) = A + B = D/V_b$ and $C_b(\infty) = B = D(V_b + V_e)$ (for $k_2 = 0$, i.e., no secretion by the kidneys) are taken into account (D is the dose of tracer). The constraints form two linear equations with the two variables A and B. The solution is

$$A = D \frac{V_e}{V_b(V_b + V_e)} \qquad B = D \frac{1}{V_b + V_e} \tag{A.5}$$

The pharmacokinetic model for the blood compartment becomes

$$C_b(t) = D\left(\frac{V_e}{V_b(V_b + V_e)} \exp\left(- \frac{k_1(V_b + V_e)}{V_b V_e} t \right) + \frac{1}{V_b + V_e} \exp\left(- \frac{k_2}{2V_b} t \right) \right) \tag{A.6}$$

As the secretion by the kidneys is slow compared with the exchange of tracer between the plasma and extracellular compartments, $k_1 \gg k_2$, Eq. (A.6) can be approximated by

$$C_b(t) \cong D\left(\frac{V_e}{V_b(V_b + V_e)} \exp\left(- \frac{k_1(V_b + V_e)}{V_b V_e} t \right) + \frac{1}{V_b + V_e} \right) \tag{A.7}$$

Appendix B

The approximation to $C_b(t)$ simplifies the derivation of the concentration function for the extracellular compartment. The concentration of tracer in this compartment is given by the differential equation [7]

$$\frac{dC_e}{dt} = \frac{PS}{V_e \nu_e}(C_b - C_e) = \frac{k}{\nu_e}(C_b - C_e) \tag{B.1}$$

with, $0 \le \nu_e \le 1$, the fraction of heavily vascularized tissue and V_e the volume of the extracellular water. P is the permeability coefficient and S the surface area of the leaking capillaries. Combining Eq. (A.7) and (B.1) yields

$$\frac{dC_e}{dt} + \frac{k}{\nu_e} C_e = \frac{k}{\nu_e} D\left(\frac{V_e}{V_b(V_b + V_e)} \exp\left(- \frac{k_1(V_b + V_e)}{V_b V_e} t \right) + \frac{1}{V_b + V_e} \right) \tag{B.2}$$

which is a first order differential equation ($y' + Qy = R$). The general solution is given by [21]

$$y = e^{-\int Q\,dt} \left[\int R e^{\int Q\,dt}\,dt + F e^{-\int Q\,dt} \right] \tag{B.3}$$

which yields

$$C_e(t) = e^{-\int (k/\nu_e)\,dt} \cdot \left[\int \left[\frac{k}{\nu_e} D\left(\frac{V_e}{V_b(V_b + V_e)} \exp\left(- \frac{k_1(V_b + V_e)}{V_b V_e} t \right) + \frac{1}{V_b + V_e} \right) \right] e^{\int (k/\nu_e)\,dt}\,dt + F e^{-\int (k/\nu_e)\,dt} \right] \tag{B.4}$$

The solution to Eq. (B.4) is

$$C_e(t) = e^{-(k/\nu_e)t} \cdot \left[\int \left[\frac{k}{\nu_e} D\left(\frac{V_e}{V_b(V_b + V_e)} \exp\left(- \frac{k_1(V_b + V_e)}{V_b V_e} t \right) + \frac{1}{V_b + V_e} \right) \right] e^{(k/\nu_e)t}\,dt + F e^{-(k/\nu_e)t} \right] \tag{B.5}$$

Eq. (B.5) simplifies to

$$C_e(t) = D\left(\frac{1}{V_b + V_e} - \frac{k}{\nu_e} \frac{V_e}{V_b(V_b + V_e)\left(k_1 \frac{V_b + V_e}{V_b V_e} - \frac{k}{\nu_e} \right)} \exp\left(- \frac{k_1(V_b + V_e)}{V_b V_e} t \right) \right) + F e^{-2(k/\nu_e)t} \tag{B.6}$$

As $C_e(0) = 0$,

$$F = -D\left(\frac{1}{V_b + V_e} - \frac{k}{\nu_e} \frac{V_e}{V_b(V_b + V_e)\left(k_1 \frac{V_b + V_e}{V_b V_e} - \frac{k}{\nu_e} \right)} \right) \tag{B.7}$$

Eq. (B.6) can be simplified into the approximate model [7,22]

$$C_e(t) \cong a(e^{-m_2 t} - e^{-m_1 t}) \tag{B.8}$$

with a an amplitude factor and $m_1 = 2k/v_e$.

Appendix C

In this appendix, we derive the formulas for registering the corresponding contours drawn in the MR and histologic images. Solely the three degrees of freedom: position, orientation and scale, are taken into account whereas foreshortening is not included. Define the contour drawn in the MR image by the ordered set of coordinates

$$C_{\mathrm{MR}} = \{(x_{1_{\mathrm{MR}}}, y_{1_{\mathrm{MR}}}), \ldots, (x_{r_{\mathrm{MR}}}, y_{r_{\mathrm{MR}}})\} \tag{C.1}$$

and the congruent contour in the histologic image by the set

$$C_{\mathrm{HI}} = \{(x_{1_{\mathrm{HI}}}, y_{1_{\mathrm{HI}}}), \ldots, (x_{v_{\mathrm{HI}}}, y_{v_{\mathrm{HI}}})\} \tag{C.2}$$

Define further the two (symmetric) covariance matrices

$$\Sigma_{\mathrm{MR}} = \begin{pmatrix} \sigma^2_{x_{\mathrm{MR}}} & \mathrm{cov}(x_{\mathrm{MR}}, y_{\mathrm{MR}}) \\ \mathrm{cov}(x_{\mathrm{MR}}, y_{\mathrm{MR}}) & \sigma^2_{y_{\mathrm{MR}}} \end{pmatrix}$$

$$\Sigma_{\mathrm{HI}} = \begin{pmatrix} \sigma^2_{x_{\mathrm{HI}}} & \mathrm{cov}(x_{\mathrm{HI}}, y_{\mathrm{HI}}) \\ \mathrm{cov}(x_{\mathrm{HI}}, y_{\mathrm{HI}}) & \sigma^2_{y_{\mathrm{HI}}} \end{pmatrix} \tag{C.3}$$

The centers of gravity of the two contours are given by

$$\begin{pmatrix} x_{0_{\mathrm{MR}}} \\ y_{0_{\mathrm{MR}}} \end{pmatrix} = \frac{1}{r} \begin{pmatrix} \sum_j x_{j_{\mathrm{MR}}} \\ \sum_j y_{j_{\mathrm{MR}}} \end{pmatrix} \qquad \begin{pmatrix} x_{0_{\mathrm{HI}}} \\ y_{0_{\mathrm{HI}}} \end{pmatrix} = \frac{1}{v} \begin{pmatrix} \sum_j x_{j_{\mathrm{HI}}} \\ \sum_j y_{j_{\mathrm{HI}}} \end{pmatrix} \tag{C.4}$$

and the translation vector by

$$\Delta p = \begin{pmatrix} \Delta x_0 \\ \Delta y_0 \end{pmatrix} = \begin{pmatrix} x_{0_{\mathrm{MR}}} \\ y_{0_{\mathrm{MR}}} \end{pmatrix} - \begin{pmatrix} x_{0_{\mathrm{HI}}} \\ y_{0_{\mathrm{HI}}} \end{pmatrix} \tag{C.5}$$

Define the eigenvalues and eigenvectors of the covariance matrices

$$\Sigma_{\mathrm{MR}} = E^{\mathrm{T}}_{\mathrm{MR}} \Lambda_{\mathrm{MR}} E_{\mathrm{MR}} \qquad \Sigma_{\mathrm{HI}} = E^{\mathrm{T}}_{\mathrm{HI}} \Lambda_{\mathrm{HI}} E_{\mathrm{HI}} \tag{C.6}$$

The difference in rotation angle is then

$$\begin{aligned} \Delta\alpha &= \arccos(e_{1,1_{\mathrm{MR}}}) - \arccos(e_{1,1_{\mathrm{HI}}}) \\ &= \arcsin(e_{1,2_{\mathrm{MR}}}) - \arcsin(e_{1,2_{\mathrm{HI}}}) \end{aligned} \tag{C.7}$$

and the difference in scale

$$\Delta S = \sqrt{\frac{1}{2}\left(\frac{\lambda_{1_{\mathrm{MR}}}}{\lambda_{1_{\mathrm{HI}}}} + \frac{\lambda_{2_{\mathrm{MR}}}}{\lambda_{2_{\mathrm{HI}}}}\right)} \tag{C.8}$$

where it is assumed that the eigenvalues $\lambda_1 \geq \lambda_2$ for both contours. The three parameters Δp, $\Delta\alpha$ and ΔS specify the transformation of the histologic mask such that it coincides with the MR image.

References

[1] Egmont-Petersen M, Pelikan E. Detection of bone tumours in radiographs using neural networks. Pattern Anal Appl 1999;2:172–83.

[2] Bloem JL, van der Woude HJ, Geirnaerdt M, Hogendoorn PC, Taminiau AH, Hermans J. Does magnetic resonance imaging make a difference for patients with musculoskeletal sarcoma? Br J Radiol 1997;70:327–37.

[3] van der Woude HJ, Verstraete KL, Hogendoorn PCW, Taminiau AHM, Hermans J, Bloem JL. Musculoskeletal Tumors: does fast dynamic contrast-enhanced subtraction MR Imaging contribute to the characterization? Radiology 1998;208:821–8.

[4] Kroon HM, Bloem JL, Holscher HC, van der Woude HJ, Reijnierse M, Taminiau AH. MR imaging of edema accompanying benign and malignant bone tumors. Skeletal Radiol 1994;23:261–9.

[5] van der Woude HJ, Bloem JL, Verstraete KL, Taminiau AH, Nooy MA, Hogendoorn PC. Osteosarcoma and Ewing's sarcoma after neoadjuvant chemotherapy: value of dynamic MR imaging in detecting viable tumor before surgery. Am J Roentgenol 1995;165:593–8.

[6] van der Woude HJ, Bloem JL, Holscher HC, Nooy MA, Taminiau AH, Hermans J, Falke TH, Hogendoorn PC. Monitoring the effect of chemotherapy in Ewing's sarcoma of bone with MR imaging. Skeletal Radiol 1994;23:493–500.

[7] Tofts PS, Kermode AG. Measurement of the blood-brain barrier permeability and leakage space using dynamic MR imaging. 1. Fundamental concepts. Magn Reson Med 1991;17:357–67.

[8] Jürgens H, Dunst J, Göbel U, et al. Improved survival in Ewing's sarcoma with response based on local therapy and intensive chemotherapy. Proc Am Soc Clin Oncol 1991. p 316.

[9] van der Woude HJ, Bloem JL, Taminiau AH, Nooy MA, Hogendoorn PC. Classification of histopathologic changes following chemotherapy in Ewing's sarcoma of bone. Skeletal Radiol 1994;23:501–7.

[10] Blombergen N. Proton relaxation times in paramagnetic solutions. J Chem Phys 1957;27:572–3.

[11] Hoffmann U, Brix G, Knopp MV, Hess T, Lorenz WJ. Pharmacokinetic mapping of the breast: a new method for dynamic MR mammography. Magn Reson Med 1995;33:506–14.

[12] Gullberg GT, Ma X, Parker DL, Ghosh Roy DN. An MRI perfusion model incorporating nonequilibrium exchange between vascular and extravascular components. Magn Reson Imaging 1991;9:39–52.

[13] Rowland M, Tozer TN. Clinical pharmacokinetics. Baltimore: Williams & Wilkins, 1995.

[14] Meyer E. Simultaneous correction for tracer arrival delay and dispersion in CBF measurements by the (H2O)-O-15 autoradiographic method and dynamic PET. J Nucl Med 1989;30:1069–78.

[15] van der Woude HJ, Bloem JL, Taminiau AH, Nooy MA, Hogendoorn PC. Treatment of high-grade bone sarcomas with neoadjuvant chemotherapy: the utility of sequential color Doppler sonography in predicting histopathologic response. Am J Roentgenol 1995;165:125–33.

[16] Press WH, Teukolsky SA, Vetterling WT, Flannery BP. Numerical recipes in C. Cambridge: Cambridge University Press, 1992.

[17] Egmont-Petersen M, Talmon JL, Brender J, McNair P. On the quality of neural net classifiers. Artificial Intelligence Med 1994;6:359–81.

[18] DeBaere T, Vanel D, Shapeero LG, Charpentier A, Terrier P, DiPaola M. Osteosarcoma after chemotherapy—Evaluation with contrast material enhanced subtraction MR Imaging. Radiology 1992;185:587–92.

[19] Wikstrom MG, Moseley ME, White DL, Dupon JW, Winkelhake JL, Kopplin J, Brasch RC. Contrast-enhanced MRI of tumors—Comparison of Gd-DTPA and a macromolecular agent. Invest Radiol 1989;24:609–15.

[20] Lyng H, Dahle GA, Kaalhus O, Skretting A, Rofstad EK. Measurement of perfusion rate in human melanoma xenografts by contrast-enhanced magnetic resonance imaging. Magn Reson Med 1998;40:89–98.

[21] Boas ML. Mathematical methods in the physical sciences. New York: John Wiley & Sons, 1983.

[22] Tofts PS, Berkowitz B, Schnall MD. Quantitative analysis of dynamic Gd-DTPA enhancement in breast tumors using a permeability model. Magn Reson Med 1995;33:564–8.